

Journal of
Mechanics of
Materials and Structures

**CYLINDRICAL INDENTATION INDUCED DEFORMATION
IN FACE-CENTERED CUBIC METAL SINGLE CRYSTALS**

Yong Xue Gan, Yuki Saito and Xi Chen

Volume 2, N° 3

March 2007

CYLINDRICAL INDENTATION INDUCED DEFORMATION IN FACE-CENTERED CUBIC METAL SINGLE CRYSTALS

YONG XUE GAN, YUKI SAITO AND XI CHEN

We investigate the deformation field induced by a cylindrical indentation on a face-centered cubic single crystal of aluminum or copper. We first present experimental measurements of the load–displacement curve and the crystal lattice rotation field (under plane strain condition) of an aluminum single crystal subject to indentation, together with related results for a copper crystal. Next, finite element simulations of the lattice rotation and displacement field associated with the cylindrical indentation are provided. The numerical and experimental results about lattice rotation features are compared with theoretical predictions based on the single crystal plasticity. Finally, the displacement fields obtained from the numerical solutions and experiments are compared. Both electron backscatter diffraction experiments using scanning electron microscopy and finite element simulations show the existence of different slip sector boundaries in the single crystals, in agreement with theoretical predictions of active slip systems and dislocation structures.

1. Introduction

As a localized impression testing technique, indentation has been extensively studied for evaluating materials properties such as the modulus [He et al. 2006], hardness [Zhang et al. 2004], fracture toughness [Tanaka et al. 2003], and creep properties [Wen et al. 2006]. Indentation has several advantages over other mechanical property testing methods, as it can be easily carried out on small specimens with minimum sample preparation [Sastry 2005a]. Compared with conical or wedge indenters, a cylindrical indenter can apply an approximately constant load to the contact region, resulting in relatively stable stress and deformation fields [Sastry 2005b]. Thus, cylindrical indentation is a very useful method to characterize the constitutive behavior of materials.

Because the mechanical properties of hard materials are difficult to obtain by conventional tension, compression or cyclic loading tests, the indentation method has recently been applied to such materials, for instance in [Guillou et al. 1993] (ceramics), [Seo et al. 2003] (surface passive films) and [Stevenson et al. 2001] (intermetallic compounds). Indentation has also been used for evaluating the deformation behavior of ductile materials [Zhu et al. 2004; Fujiwara and Otsuka 1999]. Yamada and Ikeda [1975] investigated the deformation mechanism of indentation onto the surface of a copper single crystal, finding subgrain formation on the surface and misorientation. In [Kobayashi et al. 1990], indentation tests using a steel ball were carried out on the (001), (011) and (111) faces of α -CuAl single crystals. The plastic

Keywords: indentation, single crystal, anisotropic plasticity, deformation field, lattice rotation map, numerical simulations. This work is supported by a research initiation fund from Department of Mechanical Engineering at The Cooper Union. The numerical work is supported by the National Science Foundation (CMS-0407743). The experimental work is also supported in part by Columbia Nanomechanics Research Center. We acknowledge the usage of the shared experimental facilities at Columbia University.

deformation mechanism of the surface layer under different indentation configurations was interpreted. Besides the details on slip trace distribution, the dislocation density around the indentation on the (111) and (211) planes was revealed by etching pits on the surface.

The load-displacement behavior during nanoindentation of electrodeposited single crystal copper nanowires (about 500 nm in size) was studied by Bansal et al. [2005], and compared with that of bulk nanocrystalline and annealed copper. The hardness value for extruded polycrystalline copper nanowires with 50 nm grain size was reported as 2.1 GPa; the value for single crystal copper nanowire was found to be about 1.8 GPa.

Understanding the anisotropic properties associated with indentation into face-centered cubic (FCC) single crystals is very important because the deformation field is determined by the contribution of each active slip system. Kobayashi et al. [1990] report that the slip tends to occur in the [110] direction on the (001) and (011) crystal planes if the indentation loading is applied on the (001) or (110) crystallographic plane; they also found that in the case of indentation on the (111) plane, the slip occurred on two sets of planes, located in truncated triangular pyramids, one diverging and the other converging into the single crystal. Due to plastic anisotropy, the hardness of FCC single crystals is orientation-dependent. Based on this property, a method for determining the orientation of a single crystal by indentation testing was reported in [Chang and Sheu 1992]. In that work, the orientation of the crystal was determined through an exam of the slip lines formed around the indented regions in Al-Li single crystals.

In this paper, we present the experimental, numerical and analytical results obtained from the investigation of cylindrical indentation into FCC single crystals. Aluminum and copper crystals are employed in the study because these metallic crystals possess typical elastic-plastic constitutive behaviors. The indentation patterns, such as the slip line traces generated by cylindrical indenters, are sufficiently regular and the deformation state is considerably stable.

Section 2 describes the materials and experimental procedures used. Section 3 deals with the finite element simulation method and its implementation. The indentation load-displacement relationship and the crystal lattice rotation field under plane strain conditions of an aluminum single crystal are presented in Section 4. Also in the same section, finite element (FE) simulation solutions to the lattice rotation and displacement field associated with the cylindrical indentation into face-centered cubic (FCC) single crystals are provided. Correlation among the predictions on the deformation state by the single crystal plasticity theory, the numerical FE solutions and the experimental results of the lattice rotation features is established. In the last part of Section 4, a comparison is made of the indentation displacement field obtained from numerical simulations and from experiments. Conclusions are summarized in Section 5.

2. Materials and experiments

Materials. Two types of FCC single crystals are employed in this work. The first is an aluminum single crystal of 99.999% purity, grown from melt with the seeded Bridgman technique. The direction of solidification is $[1\bar{1}4]$. The as-grown crystal was etched in a 20% (by weight) NaOH aqueous solution to remove the surface oxide layer formed at the high temperatures required for crystal growth. Laue X-ray diffraction was conducted to determine the crystallographic orientation to within $\pm 1^\circ$. After taking the X-ray image, we reoriented the Al single crystal and performed a series of cuts using an electric discharge

machine (EDM) so that the $[110]$ is the surface normal; $[\bar{1}10]$ is aligned horizontally; and $[001]$ is aligned up vertically.

The second type of FCC single crystal used is copper single crystal. Pure copper single crystal was supplied in cylindrical form with the axis oriented along $[001]$ crystallographic direction. The crystal was cut using the same electrical discharge machine, so that the (110) plane was exposed. Laue X-ray diffraction for this crystal was also conducted to confirm the orientation.

Sandpaper with various grits from No. 120 to No. 1200, supplied by Buehler, Lake Bluff, IL, were used in coarse polishing. Fabric polishing pads and diamond polishing compounds with $6\ \mu\text{m}$ and $1\ \mu\text{m}$ diamond particles, which were also acquired from Buehler, were used in fine polishing. Chemicals including hydrochloric acid and phosphoric acid in ACS standard purity were used for removing the surface oxide layer and for electrochemical polishing of the copper crystal; the chemicals were purchased from Alfa Aesar, Ward Hill, MD. The nickel(II) sulfate and nickel anode for electroplating nickel on the surface of the copper crystal were obtained from Alfa Aesar. Solvents such as trichloroethylene and acetone supplied by Alfa Aesar were used for surface degreasing of the aluminum and copper single crystals. Epoxy resin and the curing agent trademarked as DEVCON, used for bonding the single crystals, were acquired from ITW Performance Polymers, Riviera Beach, FL.

Specimen preparation. The copper and aluminum crystals were cut into $20 \times 10 \times 10\ \text{mm}^3$ blocks using the EDM. The surface to be indented was polished using grit 120, 240, 320 and 400 silicon carbide sandpaper. The surface of the single crystals was then mechanically polished following the procedures: The grit 600 sandpaper was used to grind the surface under minimum pressure along one direction until any deep scratches from the previous cutting process became invisible. During this process, water was used as lubricant and coolant to prevent the surface from being overheated. The purpose of this polishing procedure is to remove the possible deep deformation layer from the previous grinding processes. The grinding/polishing along one direction can prevent the rounded corner formation along the edges of the polished surface. The polishing direction was changed by 90° to continue polishing using the same grit 600 sand paper, but even less pressure was applied until the scratches from the previous polishing procedure became invisible. Water was supplied continuously for cooling and smooth grinding. The purpose of this polishing procedure is to remove the possible residual stress layer generated from previous polishing. The specimen was washed with tap water to prevent any coarse abrasive going into the next polishing procedure.

Subsequent mechanical polishing was conducted using a grit 1200 sand paper to polish the surface under minimum pressure along one direction until any rough scratches became invisible, lubricated by water. After this procedure, the polish direction is changed by 90° to continue polishing using a grit 1200 sand paper repetitively until the scratches from the previous procedure became invisible. This repeated procedure could help to further reduce the thickness of the surface deformation layer formed in the previous polishing procedures. In addition, changing the polishing direction helps to remove any texture built-up due to polishing along a fixed direction. After each polishing step, the specimen was washed with tap water to prevent any coarse abrasive going into the next polishing procedure.

The following procedures were applied for polishing the surface of the single crystal with diamond compound and using lapping oil as lubricant. The specimen is first polished with $6\ \mu\text{m}$ diamond paste with minimum pressure until no deep scratches were shown. The specimens were then washed in soapy

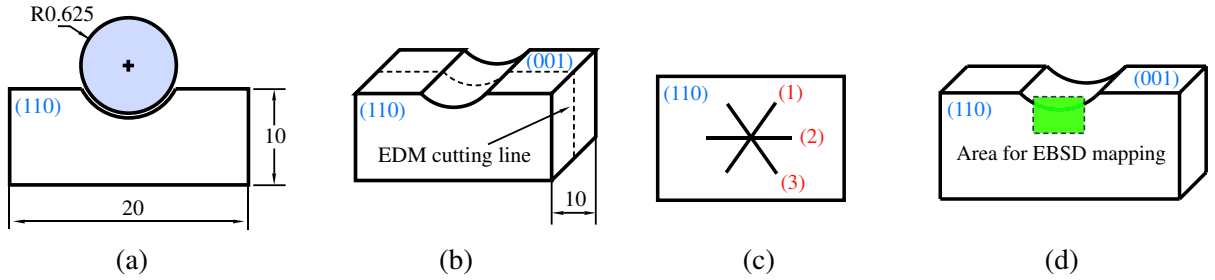


Figure 1. Schematic of cylindrical indentation experiment: (a) cylindrical indentation into Al single crystal, (b) EDM cutting for exposing the midsection of the crystal, (c) active slip systems in the single crystal under cylindrical indentation, (d) region for EBSD measurement.

water. Ultrasonic cleaning was applied to remove any attached particles from the specimen. After that, the specimens were polished using $1\ \mu\text{m}$ diamond paste with minimum pressure. The oil lubricant was applied frequently to keep a very smooth polishing condition. The polishing was done until no preferentially aligned scratches could be observed. Upon the completion of this polishing procedure, the surface of the aluminum and copper crystals show mirror luster with shiny reflection under light.

Indentation. Cylindrical indentation was performed on both aluminum and copper single crystal specimens. The indenter with a diameter of 0.625 mm as shown in Figure 1(a) was made of tungsten carbide bonded by a ferrous alloy. The indentation was under load control condition using a microindentation fixture. The loading direction was $[00\bar{1}]$ and the loading rate was approximately 5×10^{-4} mm/s. During indentation, the load and the indentation displacement data were recorded by a LabView 7.0 program and subsequently processed using a MATLAB code.

Electron microscopic examination. After the indentation, exposure of the mid-section of the single crystal specimens with plane strain deformation conditions was performed by an EDM cut as shown in Figure 1(b). After the cut, the aluminum single crystal was put into a compacted fixture and the indented area was painted with a layer of epoxy for protection. The indented (001) surface of the copper single crystal was electroplated with nickel to protect the indented region. The electrolyte and electroplating conditions for this work were adapted from the nickel-plating formula given in [Lowenheim 1978], and were as follows: nickel(II) sulfate hexahydrate, 250 g per liter; hydrochloric acid, 60 g (of 36.5% solution) per liter; temperature, 50°C ; current density, $500\ \text{A}/\text{m}^2$; time, 2 minutes. The anode was a nickel rod.

After electroplating, the copper crystal was carefully polished on the (110) plane following the same procedures described on page 559. After mechanical polish, the copper single crystal was first degreased using soapy water, then trichloroethylene, and finally acetone. The cleaned copper crystal was surface activated in a 10% HCl aqueous solution followed by rinsing in distilled water. After that, the surface of (110) of the single copper crystal was electropolished in an orthophosphoric acid solution. The composition of the solution and the detailed electropolishing procedures are given in [Ahmed et al. 1997] and [Morse 2002], respectively.

The procedures for aluminum crystal preparation are as follows: The exposed surface from the mid-section of the Al single crystal was protected by the epoxy coating and then coarse polished using 120,

240, 320 and 400 grit silicon carbide sandpaper with water as a lubricant. Further polishing using 600 and 1200 grit sandpaper was performed under minimum pressure. After that, fine polishing with 6-micron and 1-micron diamond compounds with oil as a lubricant was performed. After fine polishing with the diamond paste, electropolishing of the single crystal was conducted in an electrolyte containing 30% volume nitric acid (ACS purity, concentration 67%) and 70% volume methyl alcohol for 30 seconds at -20°C . Ultrasonic cleaning in solvents was performed after electropolishing. The specimens were then used for scanning electron microscopic (SEM) examination and electron backscatter diffraction (EBSD) measurements.

SEM examination and EBSD data acquisition at a specimen tilt angle of 70° were carried out on a JEOL 5600 scanning electron microscope. Figure 1(c) schematically shows the slip traces of the single crystals underneath the indented region. Such slip line features reveal three active slip systems as predicted by the slip line theory [Rice 1973]. Figure 1(d) is the schematic showing the region for the EBSD measurement. In Figure 2, left, the configuration of a specimen in the chamber of the microscope is shown. Figure 2, right, is an SEM micrograph taken from the indented aluminum single crystal. The area for the EBSD mapping is also shown. The typical step size for EBSD mapping is $3 \pm 0.1 \mu\text{m}$. The EBSD measurement data were analyzed using the HKL Channel 5 software. Backscatter electron (BSE) microscopic examination on selected region of copper single crystal specimens was performed at 0° specimen tilt angle using a Hitachi 4700 field emission electron microscope to determine the indentation displacement field, as will be discussed in more detail in Section 4.6.

3. Finite element simulations

Finite element analysis was performed using ABAQUS version 6.4-1. The user-material subroutine for single crystal plasticity developed by Huang [1991] and modified by Kysar [1997] was used in the implementation of finite element solutions for both aluminum and copper single crystals. The indentation contact, loading and unloading were set under displacement control to achieve better convergence than in the case of under load control. The critical shear stress for the aluminum single crystal, τ , was assumed to be 1.0 MPa. This value for copper single crystal was 58.0 MPa according to Huang [1991]. The element

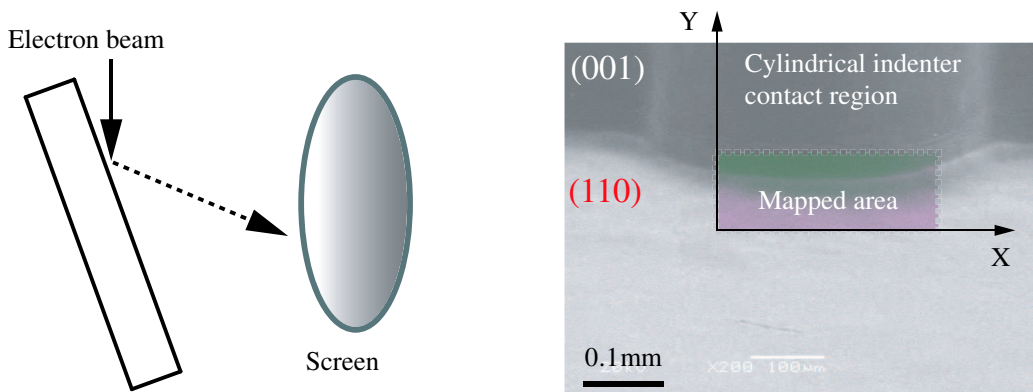


Figure 2. Illustrations of crystal lattice rotation measurement: specimen configuration and SEM image showing EBSD mapping region.

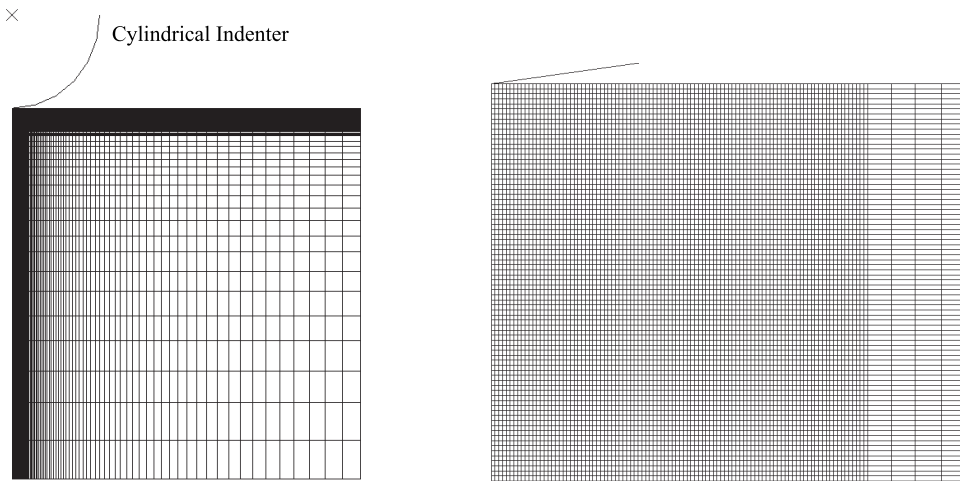


Figure 3. Schematic of the cylindrical indenter and the mesh for numerical analysis: global view (left) and detail near the tip of the indenter. (In the global view, the small mesh size collapses the lines into a band.)

used in the simulation was a plane strain reduced integration, hybrid element (CPE4RH) implemented in ABAQUS. The cylindrical indenter was defined as analytically rigid. Figure 3 shows the configuration of the cylindrical indenter and the mesh of the single crystals; note on the left-hand diagram that the density of the mesh increases drastically in the vicinity of the indenter tip. In the finite element analysis, the lattice rotation and displacements were solved incrementally by ABAQUS using a finite strain kinematic structure described by Huang [1991]. The constitutive properties were taken to be elastic-plastic. The power-law rate-dependent relationship was initially proposed by Hutchinson [1976], and described in detail in [Connolly and McHugh 1999; Huang 1991; Kysar 2001; Peirce et al. 1983; Savage et al. 2004]. The function related to the critical resolved shear stress of the k -th slip system was taken as a constant. The reference strain rate was $\dot{\gamma}_0 = 10^{-3} \text{ s}^{-1}$, and the rate sensitivity exponent $m = 50$. The Peirce–Asaro–Needleman hardening model [Peirce et al. 1983] was used in the simulation. The parameters related to the hardening were defined as in [Huang 1991]. During the simulation, the minimum iteration step used is 1×10^{-9} and the maximum step is 5×10^{-5} and approximately 20000 increments were performed in the loading simulation and unloading simulations, respectively.

4. Results and discussion

4.1. Load-displacement relation. Figure 4 shows the load-displacement curve for the aluminum single crystal, where the large hysteresis loop indicates the finite plastic deformation occurred under the cylindrical indentation. Since the deformation is dominated by plasticity, the elastic unloading region is fairly small (the right-hand part of Figure 4). The deformation behavior can be explained by the easy gliding (slip) property of an FCC single crystal under external loadings. In an FCC single crystal such as aluminum single crystal, there are 12 favorable slip systems. Under certain loading conditions, some of the slip systems become active. Thus, the plastic deformation dominated behavior is observed in

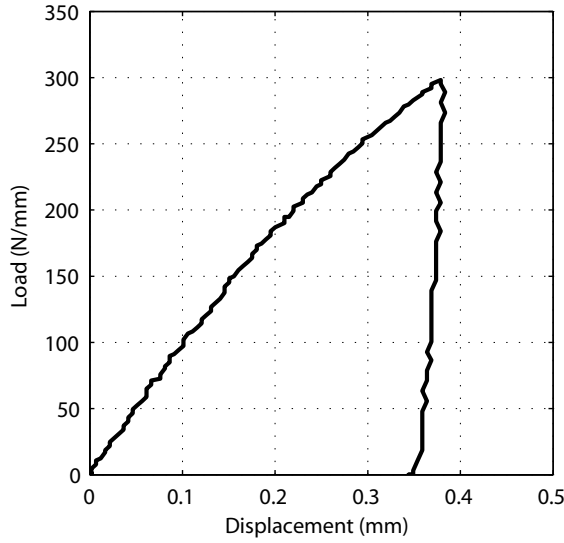


Figure 4. Load-displacement relation associated with cylindrical indentation.

Figure 4. Such plastic deformation-dominated behavior makes the experimental results of lattice rotation comparable with the slip line theory predictions, as will be discussed in detail in Section 4.4.

4.2. Crystal lattice rotation determined by EBSD measurement. Figure 5 is the out-of-plane crystal lattice rotation map for the FCC aluminum single crystal. In the indenter penetrated region, it can be seen that significant misorientation exists. This came from the severe plastic deformation of the indented plane: (001).

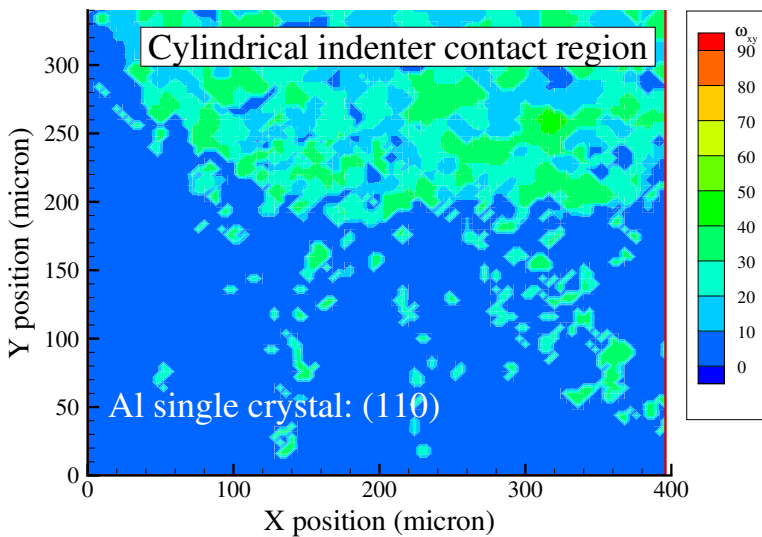


Figure 5. EBSD measurement results showing out-of-plane lattice rotation.

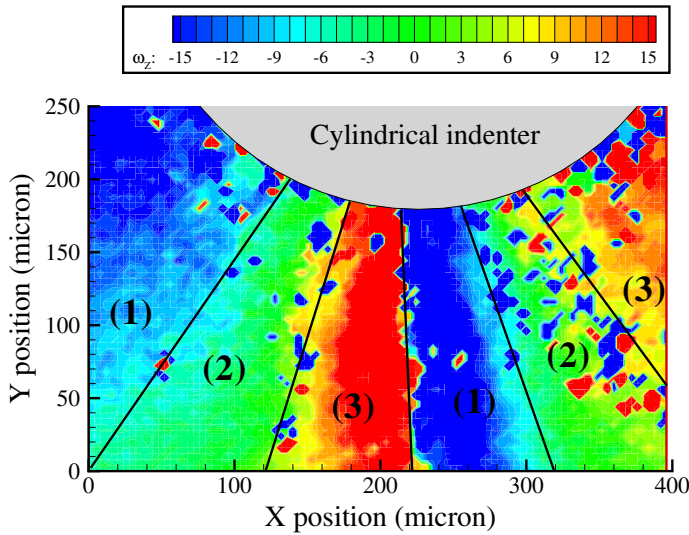


Figure 6. EBSD measurement results showing in-plane lattice rotation.

However, in the lower part of Figure 5, the original orientation of (110) plane was preserved; the out-of-plane rotation was essentially equal to zero in this region. This confirms that the midsection of the single crystal was under plane strain deformation conditions.

In Figure 6, the in-plane lattice rotation map is shown with three distinct sectors in a quadrant. The change in lattice rotation angle from one sector to another sector varies depending on the nature of the boundary. For example, from slip sector 1 to 2 and vice versa, and again from 2 to 3, the change in lattice rotation angle is about 15° . However, the change in lattice rotation is doubled when crossing the slip boundary between slip sector 1 and slip sector 3. That is why along the vertical sector boundary, as defined by Kysar et al. [2005], a “jump” in lattice rotation can be found, which was shown through experimental measurements in the region close to a microvoid within an FCC single crystal by Gan et al. [2006]. Such a sharp transition of lattice rotation along the slip boundary between the slip system 1 and slip system 3 is also revealed in this cylindrical indentation problem. The vertical line in the middle part of Figure 6 schematically shows the location at which sharp transition of crystal lattice rotation occurred. The lattice rotation results as shown in Figure 6 will be used to compare with that obtained from finite element analysis in Section 4.3.

The crystal lattice rotation results of the copper single crystal specimen are found to have the similar features as those for the aluminum single crystal. The out-of-plane rotation was essentially zero indicating that the plane strain deformation state held in the midsection of the copper single crystal. The three single slip systems are also revealed on the in-plane lattice rotation maps of the copper single crystal. Nevertheless, the in-plane lattice rotation map of the copper single crystal shows the change in rotation angle in the range of $\pm 20^\circ$ instead of $\pm 30^\circ$ for the aluminum single crystal as shown in Figure 6. Such a difference in the magnitude of lattice rotation angle may come from the difference in the critical shear strength of the two types of single crystals. The copper single crystal has a much higher critical shear strength than the aluminum single crystal. Thus the lattice rotation of the copper single crystal under the same indentation loading level is less than that of the aluminum single crystal. It is also noticed that the

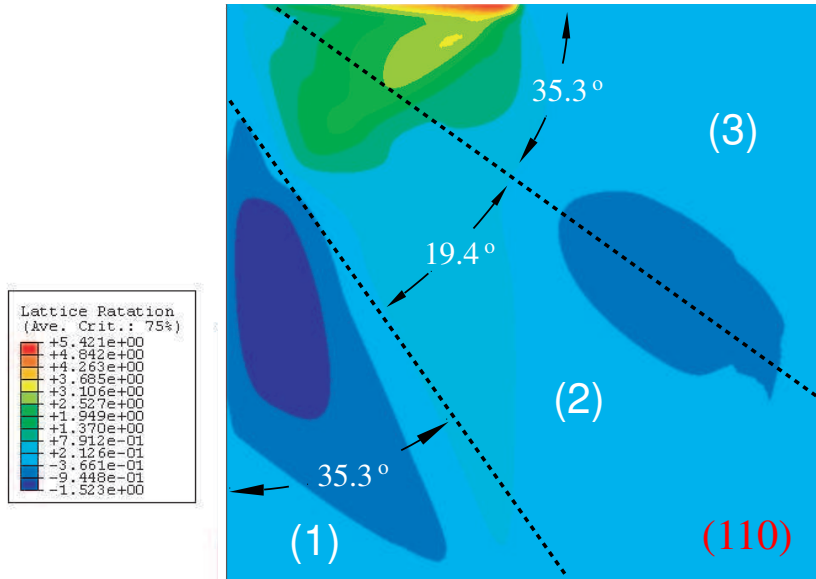


Figure 7. Numerical solution to crystal lattice rotation showing three deformation zones in a quadrant.

indenter penetration depth for the copper single crystal is much less than that for the aluminum single crystal.

4.3. Numerical solution to crystal lattice rotation. Figure 7 is the in-plane crystal lattice rotation map obtained from the finite element simulation. The unit of the lattice rotation angle is degree, which was calculated from one of the solution dependent variables (SDVs) in the ABAQUS finite element simulation program. In this case, SDV80 refers to the in-plane crystal lattice rotation. Some features of the in-plane lattice rotation from the simulation can be seen from this contour plot. In the left part of Figure 7, a region with negative lattice rotation can be found. This is due to the active dislocation movement of the slip system 1. The existence of such a negative lattice rotation region is also revealed by the experimental results as illustrated by Figure 6 in Section 4.2.

In the middle of Figure 7, the lattice rotation is close to zero. This is the region where slip system 2, with the slip direction parallel to $[\bar{1}10]$, is active. In the top-middle part of Figure 7 there is a positive lattice rotation region, caused by the active dislocation movement of slip system 3. All these features are comparable to the experimental results as shown in Figure 6. The in-plane lattice rotation predicted by the numerical simulation is in qualitative agreement with the EBSD experimental results in the sense that the three slip sectors in each quadrant are revealed. It is noted that the magnitude of the in-plane lattice rotation in the experiment is much larger than that in the simulation because a significantly larger strain was applied to the crystal specimen than in the simulation.

4.4. Correlation of the crystal lattice rotation features and the predictions by single crystal plasticity theory. The salient feature of the crystal lattice rotation as revealed by the experimental results in Section 4.2 and the numerical solutions in Section 4.3 can be explained by the single crystal plasticity theory [Schmid and Boas 1968]. In a single crystal, plastic deformation is anisotropic due to the motion of

dislocations within the crystal on discrete slip systems. Under external loading, whether a slip system is active or not is determined by Schmid’s law [1925] which states

$$n_i^{(k)} \sigma_{ij} s_j^{(k)} = \pm \tau^{(k)}, \tag{1}$$

where \mathbf{n} is the unit normal of the slip plane and \mathbf{s} is the unit vector parallel to the slip direction. σ_{ij} is the applied stress tensor and $\tau^{(k)}$ is the critical resolved shear stress of the slip system.

According to Rice [1987], in an FCC single crystal, certain slip systems may act cooperatively to allow plane strain deformation. In this case, the crystals were loaded along $[00\bar{1}]$ crystallographic direction, which causes the three slip systems active, as illustrated in Figure 8, left. There, $\mathbf{t}^{(k)}$ is the dislocation line vector of the k -th slip system with $k = 1, 2, 3$; $\mathbf{b}^{(k)}$ is the Burgers vector of the k -th slip system; $\mathbf{n}^{(k)}$ is the surface normal of the slip plane; and $\mathbf{s}^{(k)}$ is the slip direction vector. It is noted that slip system 1 corresponds to the effective slip system: $(\bar{1}\bar{1}1)[\bar{1}\bar{1}2]$, which is oriented at an in-plane angle of $\phi_1 = \tan^{-1}(\sqrt{2}) \approx 54.7^\circ$ counterclockwise relative to the $[\bar{1}\bar{1}0]$ direction. slip system 2 is parallel to the $[\bar{1}\bar{1}0]$ direction; the slip angle ϕ_2 is equal to 0. The notation slip system 3 refers to the effective slip system of $(\bar{1}\bar{1}1)[1\bar{1}2]$. It is oriented at an in-plane angle of $\phi_3 = -\tan^{-1}(\sqrt{2}) \approx -54.7^\circ$ relative to the $[\bar{1}\bar{1}0]$ direction.

Under plane strain conditions ($\sigma_{13} = \sigma_{23} = 0$), Equation (1) can be expanded as

$$(s_1 n_2 + s_2 n_1) \sigma_{12} + 2s_1 n_1 \frac{(\sigma_{11} - \sigma_{22})}{2} = \pm \tau. \tag{2}$$

If \mathbf{n} and \mathbf{s} in the crystal are projected onto the $x_1 - x_2$ plane of the crystal and rescaled as unit vectors \mathbf{N} and \mathbf{S} , respectively, Equation (2) can be rewritten as

$$(S_1 N_2 + S_2 N_1) \sigma_{12} + 2S_1 N_1 \frac{(\sigma_{11} - \sigma_{22})}{2} = \pm \beta_k \tau, \tag{3}$$

where β_k is a constant specific to the slip system under consideration such that (2) and (3) are equivalent

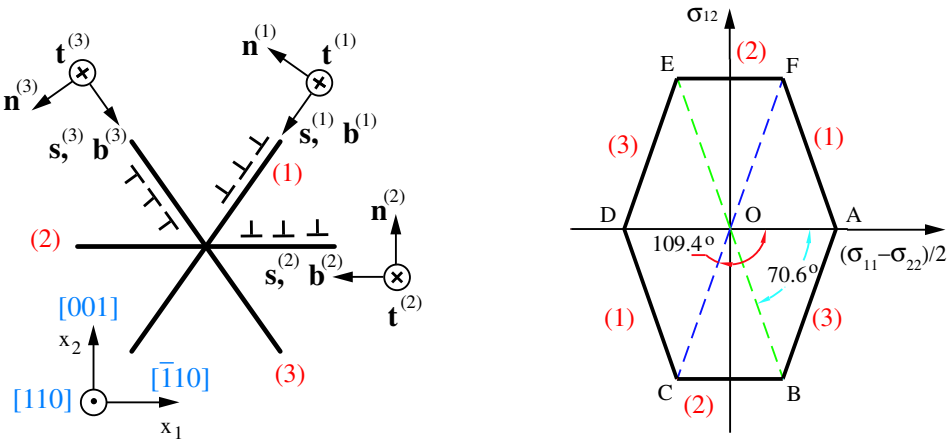


Figure 8. Schematic drawing for micromechanics analysis: configuration of the three active slip systems (left) and yield surface (right).

expressions. Rice [1987] noted that $\beta_1 = \beta_3 = 2/\sqrt{3}$ and that $\beta_2 = \sqrt{3}$ for face-centered cubic crystals. The sign for β_k depends on whether the slip system is activated in positive or negative sense.

Since $S_1 = \cos \phi_k$, $S_2 = \sin \phi_k$, $N_1 = -S_2$ and $N_2 = S_1$, Equation (3) can be simplified as

$$\sigma_{12} = \tan 2\phi_k \left(\frac{\sigma_{11} - \sigma_{22}}{2} \right) \pm \frac{\beta_k \tau}{\cos 2\phi_k}. \quad (4)$$

The above yield conditions can be plotted in stress space for each of the three effective slip systems. A hexagonal yield surface is obtained as shown in Figure 8, right. The positions of the vertices of the yield surface are as follows:

Vertex	A	B	C	D	E	F
$\frac{\sigma_{11} - \sigma_{22}}{2\tau}$	$\frac{\sqrt{6}}{2}$	$\frac{\sqrt{6}}{4}$	$-\frac{\sqrt{6}}{4}$	$-\frac{\sqrt{6}}{2}$	$-\frac{\sqrt{6}}{4}$	$\frac{\sqrt{6}}{4}$
σ_{12}	0	$-\sqrt{3}$	$-\sqrt{3}$	0	$\sqrt{3}$	$\sqrt{3}$

On the yield surface, the angle AOB equals to 70.6° . This defines the angular sector region in physical space. Since a θ degree angular region in physical space corresponds to a 2θ degree angular region in stress space, the region defined as slip system 3 takes 70.6° in the stress space as shown by the angle AOB in Figure 8, right. Thus, the slip system 3 can be determined in physical space as a circular region defined by $0 \leq \theta \leq 35.3^\circ$. Such a prediction to the existence of slip system 3 and its exact location in physical space from the single crystal plasticity theory can be confirmed by the experimental result of Figure 6. In the right-hand part of the figure, the positive in-plane crystal lattice rotation region (red-colored region) takes about a 35.3° angular region. In the right-hand part of Figure 7 (numerical solutions), a similar positive lattice rotation region can be seen. The angle COB shown in Figure 8, right, is the active region for slip system 2 in stress space. This region can be mapped into physical space as the angular region $35.3^\circ \leq \theta \leq 54.7^\circ$, which defines slip sector 2 in physical space. Similarly, the angular region $54.7^\circ \leq \theta \leq 90^\circ$ is determined as slip sector 3. The locations for slip sector 2 and slip sector 3 are also found in experiments. The experimental results are given in Figure 6. The numerical solutions as shown in Figure 7 reveals such single slip regions. Therefore, the results from experiments and simulations are in agreement with the analytical predictions.

It is also indicated that such a consistency is in a qualitative sense, because the single crystal plasticity theory assumes the crystal is rigid-ideally plastic. Also assumed here is that the yield surface as shown in Figure 8 holds at the incipient stage of yielding, where essentially no hardening behavior is considered. However, in the finite element simulation, a small strain hardening was imposed to ensure the numerical convergence. In the cylindrical indentation experiment, considerably large deformation was observed. Although the average behavior as revealed by the load-displacement relation in Figure 4 is elastic-plastic, localized strain hardening and strain gradient exist [Gan 2005]. That is why the regions related to the slip system 1 and slip system 2 shrinks in the EBSD map of Figure 6. The actual measured slip sectors from the active motion of the slip systems 1 and 2 are smaller than the analytical predictions due to the sink-in of the crystal under large scale deformation and associated strain hardening.

4.5. Numerical solutions to displacements. Finite element solutions for the 2-D displacement fields were obtained for FCC single crystals. The results from the simulations for aluminum single crystals are shown in Figure 9: horizontal displacement on the left and vertical displacement on the right. Qualitatively, both copper and aluminum have the same salient features in their indentation displacement fields. The deformed state of the crystal under the cylindrical indentation is shown in a magnified way and a factor of 10 was used to generate the plots in Figure 9. In the left half, the blue color stands for the zero displacement along x -axis, while the red colored region reveals the greatest displacement along positive x -axis. It can be seen that the region close to the indenter tip has zero horizontal movement, due to the symmetrical deformation of the crystals under indentation.

In Figure 9, right, yellow-green indicates zero displacement along the y -axis, blue indicates the negative vertical displacement and red positive vertical displacement. It is evident that materials adjacent to the indenter tip move downward, while the contact region far away from the indenter tip shows the pile-up feature of the single crystals as illustrated in the upper right part of the figure.

4.6. Comparison of displacement fields between numerical solutions and experimental results. The displacement fields associated with the cylindrical indentation into a copper single crystal were measured experimentally. As shown in Figure 10(a), on the (110) plane of a well-polished copper single crystal, regularly aligned patterns were generated by thin film technologies. First, a thin layer of photosensitive polymer (a positive photoresist, AZ5412) was spin coated on the (110) plane with a thickness of $0.6\ \mu\text{m}$. Next, a photoresist was baked on a hot plate at 105°C for 3 minutes. Subsequently, UV photolithography was employed over a mask for 15 seconds. The mask has regularly aligned $5\ \mu\text{m} \times 5\ \mu\text{m}$ chromium patterns with a separation distance of $12.5\ \mu\text{m}$. After UV exposure, a 1:4 diluted AZ400K aqueous solution was used as a developer to obtain the microscale arrays of pattern. The following step was to evaporate a gold thin film with a thickness of $0.02\ \mu\text{m}$ on the patterned polymeric layer. Since some part of the copper single crystal was covered by the polymer, while the other part was not covered by the polymer due to the photolithography process, gold coating only partially covered the (110) plane of the copper single crystal. By soaking the gold coated single crystal into acetone for 30 seconds, the polymer

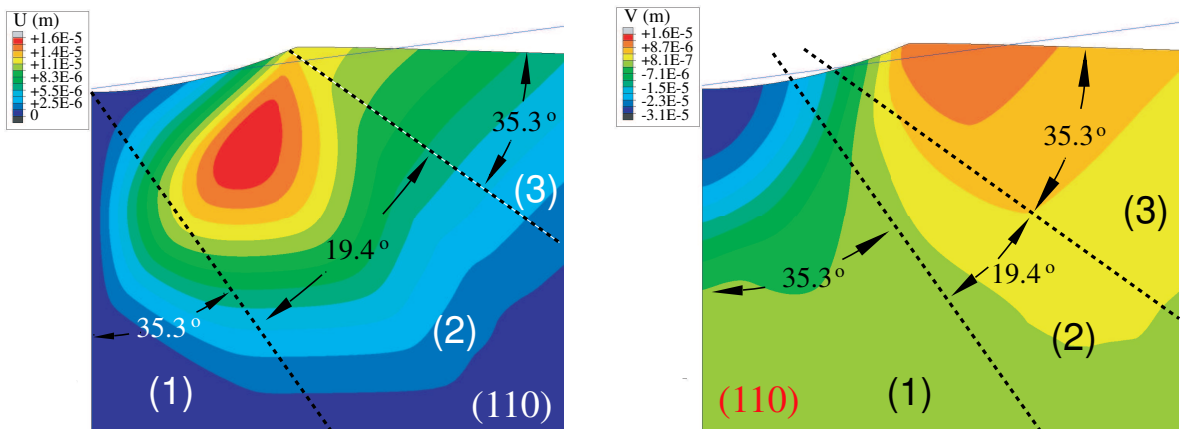


Figure 9. Horizontal (left) and vertical (right) components of numerical solution for the displacement field.

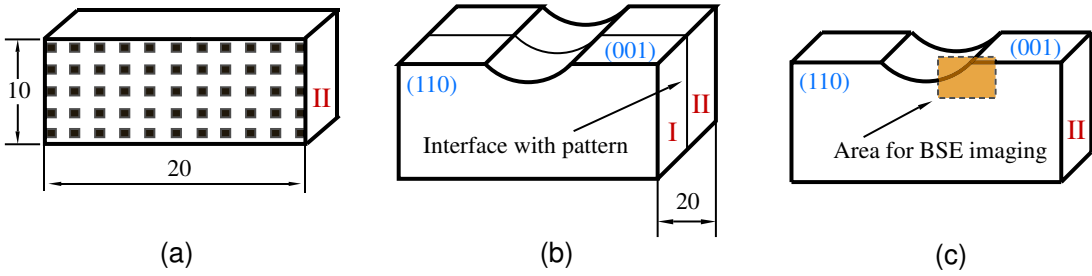


Figure 10. Experiments for measuring displacement field: (a) generating gold pattern on the (110) crystallographic plane of the single crystal, (b) cylindrical indentation into the two pieces of the single crystal, (c) imaging selected indentation area.

coating (photoresist) was peeled off from the surface of the single crystal. While in the part with gold directly being deposited on the single crystal, the gold coating was kept and the microscale square arrays formed, as schematically shown in Figure 10(a).

During cylindrical indentation, two pieces of single crystals with the same dimension were stacked together so that the two surfaces of the two pieces of crystals with microscale pattern were facing together as shown in Figure 10(b). This configuration kept the deformation state of the interface with microscale pattern under the plane strain conditions. After indentation, a selected region as shown in Figure 10(c) was examined using a Hitachi 4700 field emission electron microscope. A backscatter electron micrograph is shown in Figure 11.

The displacement fields as shown in Figure 11 are comparable to that in Figure 9. For example, the vertically aligned microscale patterns shift right with the increase of distance from the indenter tip.

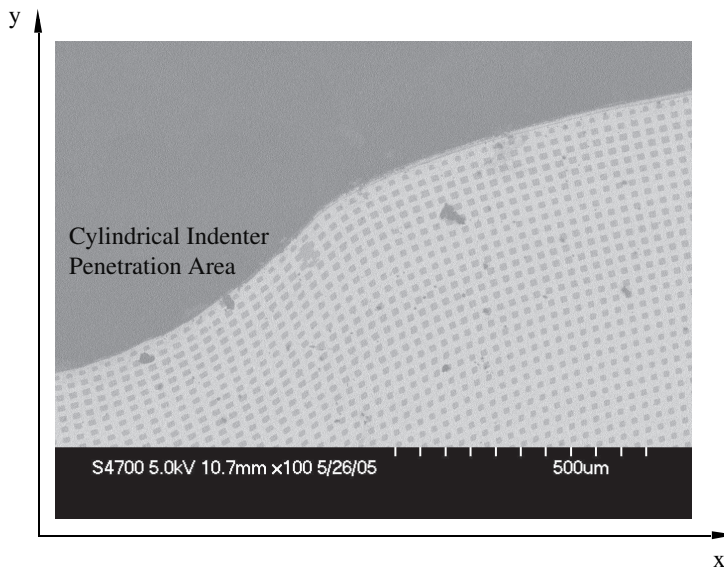


Figure 11. Backscatter scanning electron micrograph showing the plane strain deformation state.

This means that positive x -displacements exist, which is in agreement with the trends predicted by the finite element analysis results of Figure 9, left. In view of the vertical displacement, in the region underneath the cylindrical indenter, the experimental results are consistent with the numerical solutions. Negative vertical displacements are observed because of the sink-in of the single crystal under indentation loading along $-y$ direction. The difference in the vertical displacement results between the finite element simulations and the experiments is as follows: The numerical solutions predict a significant pile-up in the area underneath the right part of the indenter as shown by the positive displacement region in Figure 9, right. Nevertheless, the experimental results just show sink-in behavior, and no region of positive vertical displacement can be found in Figure 11.

Measurement of both the lattice rotation field and displacement field is essential for determining the stretching components and rotational components of a deformation gradient tensor. The results of the crystal lattice rotation in Figures 5 and 6 are helpful in determining the lattice curvature tensor as defined by Nye [1953]. From the lattice curvature tensor a correlation between the crystal lattice rotation tensor and the deformation gradient tensor can be established. For the displacement fields shown in Figure 11, they can be used to establish an explicit relationship with the stretching components of the deformation tensor. Therefore, the lattice rotation field along with the displacement field provides a significant amount of knowledge about the single crystals' plastic deformation states under cylindrical indentation.

5. Conclusions

Based on the studies of cylindrical indentation induced deformation fields in face-centered cubic aluminum and copper single crystals, the following concluding remarks can be made.

1. The indentation load-displacement relationship shows plastic deformation dominated behavior of the single crystals under cylindrical indentation.
2. Crystal lattice rotation field determined experimentally under plane strain conditions of the FCC single crystals reveals three slip sectors, which is in agreement with the qualitative features determined by finite element simulations. The lattice rotation features can also be correlated to the predictions to the deformation field based on the single crystal plasticity theory.
3. The displacement field determined by the numerical simulations also reveals the existence of different slip sector boundaries in the single crystals.
4. Comparison on the displacement field between the numerical solutions and the experimental results shows consistency in main features. The numerical solutions predict a significant pile-up in the area underneath the right part of the cylindrical indenter as shown by a positive vertical displacement region. However, the experimental results just show sink-in behavior; no region of positive vertical displacement was found.
5. Measurement of both lattice rotation field and displacement field is essential for determining the stretching components and rotational components of a deformation gradient tensor. The results of the crystal lattice rotation as obtained in this work is helpful to establish a correlation between the crystal lattice rotation tensor and the deformation gradient tensor. The displacement results can be used to determine the stretching components of the deformation tensor. Therefore, the lattice rotation field and the displacement field provide insight into the plastic deformation state of the FCC single crystals under cylindrical indentation.

References

- [Ahmed et al. 1997] J. Ahmed, A. J. Wilkinson, and S. G. Roberts, "Characterizing dislocation structures in bulk fatigued copper single crystals using electron channeling contrast imaging (ECCI)", *Philos. Mag. Lett.* **76**:4 (1997), 237–246.
- [Bansal et al. 2005] S. Bansal, E. Toimil-Molares, A. Saxena, and R. R. Tummala, "Nanoindentation of single crystal and polycrystalline copper nanowires", pp. 71–76 in *Proceedings of the 55th Electronic Components and Technology Conference* (Lake Buena Vista, FL), vol. 1, IEEE, Piscataway, NJ, 2005.
- [Chang and Sheu 1992] S. C. Chang and T. S. Sheu, "Determination of Al-Li crystal orientation by indentation", *Mater. Sci. Eng. A* **150**:1 (1992), L11–L12.
- [Connolly and McHugh 1999] P. Connolly and P. E. McHugh, "Fracture modelling of WC-Co hardmetals using crystal plasticity theory and the Gurson model", *Fatigue Fract. Eng. Mater. Struct.* **22**:1 (1999), 77–86.
- [Fujiwara and Otsuka 1999] M. Fujiwara and M. Otsuka, "Characterization of micro-indentation creep in β -Sn single crystals at elevated temperatures", *J. Jpn. Inst. Met.* **63** (1999), 760–769.
- [Gan 2005] Y. X. Gan, *High strain gradient plasticity of single crystals: theory, simulations and experiments*, Ph.D. thesis, Columbia University, New York, 2005.
- [Gan et al. 2006] Y. X. Gan, J. W. Kysar, and T. L. Morse, "Cylindrical void in a rigid-ideally plastic single crystal, II: Experiments and simulations", *Int. J. Plast.* **22**:1 (2006), 39–72.
- [Guillou et al. 1993] M.-O. Guillou, J. L. Henshall, and R. M. Hooper, "Indentation cyclic fatigue of single-crystal magnesium oxide", *J. Am. Ceram. Soc.* **76**:7 (1993), 1832–1836.
- [He et al. 2006] L. H. He, N. Fujisawa, and M. V. Swain, "Elastic modulus and stress-strain response of human enamel by nano-indentation", *Biomaterials* **27**:24 (2006), 4388–4398.
- [Huang 1991] Y. Huang, "A user-material subroutine incorporating single crystal plasticity in the ABAQUS finite element program", Division of Engineering and Applied Sciences, Harvard University, Cambridge, MA, 1991. Mech report 178.
- [Hutchinson 1976] J. W. Hutchinson, "Bounds and self-consistent estimates for creep of polycrystalline materials", *Proc. R. Soc. Lond. A* **348**:1652 (1976), 101–127.
- [Kobayashi et al. 1990] S. Kobayashi, T. Harada, and S. Miura, "Mechanism of deformation in α Cu-Al single crystals by spherical indenter, I: Simple indentation", *J. Soc. Mater. Sci. (Japan)* **39** (1990), 126–131.
- [Kysar 1997] J. W. Kysar, "Addendum to 'A user-material subroutine incorporating single crystal plasticity in the ABAQUS finite element program: Mech report 178'", Division of Engineering and Applied Sciences, Harvard University, Cambridge, MA, 1997.
- [Kysar 2001] J. W. Kysar, "Continuum simulations of directional dependence of crack growth along a copper/sapphire bicrystal interface, I: Experiments and crystal plasticity background", *J. Mech. Phys. Solids* **49**:5 (2001), 1099–1128.
- [Kysar et al. 2005] J. W. Kysar, Y. X. Gan, and G. Mendez-Arzuza, "Cylindrical void in a rigid-ideally plastic single crystal, I: Anisotropic slip line theory solution for face-centered cubic crystals", *Int. J. Plast.* **21**:8 (2005), 1481–1520.
- [Lowenheim 1978] A. F. Lowenheim, *Electroplating*, McGraw-Hill, New York, 1978.
- [Morse 2002] T. L. Morse, "Measuring lattice rotation induced by plastic deformation in single crystals", Columbia University, New York, 2002. MRSEC REU student research report.
- [Nye 1953] J. F. Nye, "Some geometrical relations in dislocation solids", *Acta Metall.* **1**:2 (1953), 153–162.
- [Peirce et al. 1983] D. Peirce, R. J. Asaro, and A. Needleman, "Material rate dependence and localised deformation in crystalline solids", *Acta Metall.* **31**:12 (1983), 1951–1976.
- [Rice 1973] J. R. Rice, "Plane strain slip line theory for anisotropic rigid-plastic materials", *J. Mech. Phys. Solids* **21**:2 (1973), 63–74.
- [Rice 1987] J. R. Rice, "Tensile crack tip fields in elastic-ideally plastic crystals", *Mech. Mater.* **6**:4 (1987), 317–335.
- [Sastry 2005a] D. H. Sastry, "Impression creep technique: an overview", *Mater. Sci. Eng. A* **409**:1–2 (2005), 67–75.
- [Sastry 2005b] D. H. Sastry, "On some investigations with the impression creep technique", Talk presented at 134th Annual Meeting and Exhibition of the TMS (San Francisco), 2005.

- [Savage et al. 2004] P. Savage, B. P. O. Donnell, P. E. McHugh, B. P. Murphy, and D. F. Quinn, "Coronary stent strut size dependent stress-strain response investigated using micromechanical finite element models", *Ann. Biomed. Eng.* **32**:2 (2004), 202–211.
- [Schmid 1925] E. Schmid, pp. 342 in *Proceedings of the First International Congress of Applied Mechanics* (Delft, 1924), edited by C. B. Biezeno and J. M. Burgers, Waltman, Delft, 1925.
- [Schmid and Boas 1968] E. Schmid and W. Boas, *Plasticity of crystals with special reference to metals*, Chapman and Hall, London, 1968.
- [Seo et al. 2003] M. Seo, M. Chiba, and Y. Kurata, "Nano-indentation to the passive metal surfaces in solution", *Corros. Eng.* **52** (2003), 5–11.
- [Stevenson et al. 2001] M. E. Stevenson, M. L. Weaver, and R. C. Bradt, "Microhardness anisotropy and the indentation size effect in single crystal NiAl", in *High-temperature ordered intermetallic alloys, IX: 2000 Fall MRS Symposium N* (Boston, 2000), edited by J. H. Schneibel et al., Materials Research Society Symposia Proceedings **646**, Materials Research Society, Warrendale, PA, 2001. Paper N6.4.
- [Tanaka et al. 2003] M. Tanaka, K. Higashida, H. Nakashima, H. Takagi, and M. Fujiwara, "Fracture toughness evaluated by indentation methods and its relation to surface energy in silicon single crystals", *Mater. Trans. (JIM)* **44**:4 (2003), 681–684.
- [Wen et al. 2006] S. P. Wen, F. Zeng, Y. Gao, and F. Pan, "Indentation creep behavior of nano-scale Ag/Co multilayers", *Scr. Mater.* **55**:2 (2006), 187–190.
- [Yamada and Ikeda 1975] A. Yamada and M. Ikeda, "Misorientation of crystal sub-grains at the indentation on Cu single crystal", *Bull. Jpn. Soc. Precis. Eng.* **9**:22 (1975), 53–54.
- [Zhang et al. 2004] Z. F. Zhang, Z. M. Sun, H. Zhang, and H. Hashimoto, "Micron-scale deformation and damage mechanisms of Ti_3SiC_2 crystals induced by indentation", *Adv. Eng. Mater.* **6**:12 (2004), 980–983.
- [Zhu et al. 2004] T. Zhu, J. Li, K. J. Van Vliet, S. Ogata, S. Yip, and S. Suresh, "Predictive modeling of nanoindentation-induced homogeneous dislocation nucleation in copper", *J. Mech. Phys. Solids* **52**:3 (2004), 691–724.

Received 24 Jul 2006. Accepted 9 Oct 2006.

YONG XUE GAN: gan@cooper.edu

Department of Mechanical Engineering, Albert Nerken School of Engineering, The Cooper Union for the Advancement of Science and Art, 51 Astor Place, New York, NY 10003, United States

and

Columbia Nanomechanics Research Center, Department of Civil Engineering and Mechanics, 622 Mudd Building, Columbia University, New York, NY 10027, United States

YUKI SAITO: ys2121@columbia.edu

Columbia Nanomechanics Research Center, Department of Civil Engineering and Mechanics, 622 Mudd Building, Columbia University, New York, NY 10027, United States

XI CHEN: xichen@civil.columbia.edu

Department of Civil Engineering and Engineering Mechanics, Fu Foundation School of Engineering and Applied Science, Columbia University, 500 West 120th Street, New York, NY 10027, United States